Micromechanics-based identification of a ductile fracture model for three structural steels

Sondre Bergo [a,b,*], David Morin [a,b], Tore Børvik [a,b] and Odd Sture Hopperstad [a,b]

[a] Structural Impact Laboratory (SIMLab), Department of Structural Engineering, Norwegian University of Science and Technology (NTNU), NO-7491 Trondheim, Norway

[b] Centre for Advanced Structural Analysis (CASA), NTNU, NO-7491 Trondheim, Norway

Abstract

From an engineering point of view, it is beneficial to reduce the number of mechanical tests required to calibrate the plasticity and fracture models of a structural material. In this study, the ductile fracture model for three high-strength steels is identified based on unit cell simulations, metal and porous plasticity modelling, and strain localization analysis combined with a single uniaxial tensile test per material. Finite element simulations of a unit cell model with a spherical void are performed with the matrix material described by metal plasticity and used to calibrate the parameters of the porous plasticity model. Strain localization analyses are conducted using the imperfection band approach with metal plasticity outside and porous plasticity inside the imperfection band. These simulations are first used to determine the nucleation rate in the porous plasticity model giving the experimentally obtained fracture strain in uniaxial tension, and then to compute the fracture locus under proportional loading in generalized axisymmetric tension. By combining the fracture locus with a simple damage accumulation rule and metal plasticity, finite element simulations of ductile fracture in tensile tests on smooth and notched specimens of the three steels are performed. Comparison of the predicted results with existing experimental data shows that the fracture model gives satisfactory estimates of ductility for a wide range of stress triaxiality ratios in steels of different strengths. This study shows the potential of micromechanical analyses in the calibration of fracture models for engineering applications.

Keywords: strain localization, unit cell simulations, Gurson model, fracture locus

*Corresponding author: Sondre Bergo (sondre.bergo@ntnu.no)

Nomenclature

Abbreviations	
FE	Finite Element
HC	Hosford-Coulomb
JC	Johnson-Cook
MMC	Modified Mohr-Coulomb
Symbols - Latin	
A_{n}	Nucleation rate
$\boldsymbol{A}^{\mathrm{t}}$	Acoustic tensor
$\boldsymbol{C}^{\mathrm{t}}$	Material tangent stiffness tensor
$\boldsymbol{D}$	Rate-of-deformation tensor
$\boldsymbol{D}^{\mathrm{p}}$	Plastic rate-of-deformation tensor
D	Damage variable
E	Young's modulus
$\boldsymbol{E}$	Macroscopic strain tensor
E_{eq}	Macroscopic equivalent strain
E_{f}	Macroscopic failure strain
$\boldsymbol{F}$	Deformation gradient tensor
f	Void volume fraction
f_{n}	Void volume fraction due to void nucleation
f_0	Initial void volume fraction
L	Lode parameter
$\boldsymbol{L}$	Velocity gradient tensor
$\boldsymbol{n}$	Unit normal vector to imperfection band
p	Equivalent plastic strain
$\boldsymbol{P}$	Nominal stress tensor
p_{f}	Equivalent plastic strain at failure
T	Stress triaxiality
q_1, q_2, q_3	Tvergaard parameters
$\dot{\boldsymbol{q}}$	Non-uniformity rate vector
Q_i, C_i	Isotropic hardening parameters
w	Unit cell void aspect ratio
Symbols - Greek	
Φ	Yield function
λ	Unit cell aspect ratio
ν	Poisson's ratio
$\boldsymbol{\sigma}$	Cauchy stress tensor
$\boldsymbol{\sigma}'$	Deviatoric part of Cauchy stress tensor
$\boldsymbol{\Sigma}$	Macroscopic stress tensor
σ_0	Initial yield stress
σ_h	Hydrostatic stress
σ_{eq}	von Mises equivalent stress
σ_{M}	Matrix flow stress

1. Introduction

In large-scale finite element simulation of steel structures subjected to accidental loads, such as impact and explosion, uncoupled plasticity and damage models are commonly used, e.g. [1]–[4]. In such models, the damage has no influence on the elastoplastic behaviour before a critical damage level is reached and the structure fails. Failure is typically modelled by element erosion. Damage reduces the load-carrying capacity of the material and leads to reduced strength and eventually strain softening, but this effect is often negligible in metals until the material is close to fracture. Dunand and Mohr [5] compared the results obtained by the uncoupled modified Mohr–Coulomb (MMC) fracture model [6] and the coupled shear-modified Gurson model [7][8] with fracture experiments over a wide range of stress triaxiality ratios and Lode angles on a TRIP-assisted steel sheet. Both models were found to be capable of predicting the fracture displacement for different stress states, but the MMC fracture model gave somewhat more accurate results. Grimsmo et al. [9] carried out finite element simulations of ductile failure of fillet-welded structural steel components using the uncoupled Cockcroft-Latham fracture model [10] and the coupled shear-modified Gurson model [7][8]. The shear-modified Gurson model was found to give results in better accordance with the experiments, which could be expected due to the simplicity of the one-parameter Cockcroft-Latham fracture model. In practical use, the main advantage of the uncoupled damage models is that they can be calibrated independently from the plasticity model, which simplifies the parameter identification from test data [11].

The main damage mechanism in ductile fracture of steel is nucleation, growth and coalescence of microscopic voids, where voids are nucleated at inclusions and second-phase particles [12]. These processes are highly dependent upon the stress state [13][14], which is often expressed in terms of the stress triaxiality and the Lode parameter. While the stress triaxiality signifies the degree of hydrostatic tension, the Lode parameter represents the deviatoric stress state. Early research on the effect of the stress triaxiality on the ductility of steel includes the studies of Hancock and co-workers [15]–[17] and Johnson and Cook [18], and later numerous studies have documented the importance of this stress state parameter, e.g. [19]–[24]. The general trend is that the ductility decreases with increasing stress triaxiality when the Lode parameter and other loading parameters are kept constant. More recently, the effect of the Lode parameter on ductile fracture in steels has been examined experimentally in several studies, e.g. [11][13][22]. Micromechanical simulations (e.g. [25]–[27]) indicate that the lowest ductility tends to occur for generalized shear

states and that the ductility is somewhat higher in generalized axisymmetric compression than in generalized axisymmetric tension.

Fracture models for steels and other metallic materials are often defined by a fracture locus valid for proportional loading conditions and a damage evolution rule that accounts for the effects of non-proportionality in the loading process. The Johnson-Cook (JC) fracture model [18], the more recent MMC [6] and Hosford–Coulomb (HC) [28] fracture models are constructed this way, where the latter fracture model was motivated from micromechanical simulations [26]. Whereas the MMC and HC fracture models depend on the stress triaxiality and the Lode parameter, the JC fracture model only accounts for stress triaxiality in addition to strain rate and temperature. In other fracture models, like the Cockcroft-Latham fracture model [10] and the extended Cockcroft-Latham fracture model [29], damage is driven by the plastic dissipation amplified by a factor that depends on the stress state via the stress triaxiality and the Lode parameter. In the original and extended Cockcroft-Latham fracture models, the fracture locus valid for proportional loading is not used in the definition of damage but can be constructed as soon as the fracture model has been calibrated.

The identification of the fracture parameters from experimental results is a complex and time-consuming process that involves finite element simulation of the tests to establish the stress and strain history at the critical point where fracture is assumed to initiate [30]. If the fracture model depends on both the stress triaxiality and the Lode parameter, many tests are required to fill the stress space in a reasonable manner even for quasi-static and isothermal conditions. If the dependence of the Lode parameter is neglected, the number of tests can be reduced, but still tests at several levels of stress triaxiality should be carried out. To readily obtain the fracture locus, it is important to design specimens that give reasonably proportional loading conditions. This is not an easy task [31] and typically significant non-proportionality occurs due to diffuse and local necking modes. As a result, inverse modelling is often used to identify the fracture parameters, applying finite element simulations of the tests with a calibrated plasticity model [32].

An alternative approach, which is explored in the study presented here, is to combine experiments with micromechanics-based modelling and thus reduce the need for experiments. Morin et al. [33] combined unit cell simulations, metal and porous plasticity modelling, and strain localization analyses to predict failure of a structural steel under moderately and strongly

proportional loadings. Results in good agreement with the experiments of Basu and Benzerga [24] were obtained. In this study, we have extended the approach used in Morin et al. [33] to allow for simulation of ductile fracture and crack propagation in finite element analyses using J_2 metal plasticity combined with a ductile fracture model calibrated based on a micromechanical approach. Despite the CPU efficiency of the strain localization analyses reported by Morin et al. [27], this technique cannot be used during run-time of a finite element analysis. Therefore, to benefit from the accuracy of this approach the calibration of a ductile fracture model is the best alternative with today's computers. The micromechanics-based modelling framework is applied to predict the fracture locus of three structural steels with different yield strength. The micro-mechanical parameters are calibrated based on unit cell simulations and a single uniaxial tension test, and localization analyses combining metal and porous plasticity models are used to calculate the fracture locus. By combining the fracture locus with a damage evolution rule, an uncoupled plasticity and damage model is obtained and then applied in simulations of tension tests on notched specimens where the dominant loading mode is axisymmetric tension. Element erosion is used to describe crack propagation. The results are compared with the experiments presented in Dey et al. [21]. It should be noted here that the proposed calibration procedure is quite general and can be used for other types of fracture models, e.g. the MMC and HC fracture models. It is, however, important to stress that the accuracy of the approach depends critically on the quality of the porous plasticity model employed in the localization analyses.

2. Materials

Three steel materials are considered in this study, namely Weldox 460E, Weldox 700E and Weldox 900E with minimum yield strength of 460 MPa, 700 MPa and 900 MPa, respectively. Weldox is a class of structural steels that combines high strength and ductility. Dey et al. [21] performed three series of tensile tests on these materials, namely quasi-static tests with smooth and notched specimens, quasi-static tests at elevated temperatures, and dynamic tests over a wide range of strain rates.

We only address the quasi-static tests on the smooth and notched specimens at room temperature in the present numerical study. The geometry of the specimens is shown in Figure 1. Notched specimens with notch radius R equal to 4 mm, 2 mm, 0.8 mm and 0.4 mm were tested, and these tests will be referred to as R4, R2, R08 and R04, respectively. All specimens were taken

parallel to the rolling direction of the steel plate. The possible anisotropy of the Weldox steel plates was not investigated experimentally by Dey et al. [21]. However, tensile tests in three material directions of the Weldox 460E steel plates performed by Børvik et al. [34] gave no indications of planar anisotropy while a slight normal anisotropy was found. Any anisotropy in the behaviour of the Weldox steels will be neglected in the numerical simulations conducted herein, in the same manner as in Børvik et al. [34] and Dey et al. [21]. The different notches induce different levels of hydrostatic tension in the minimum cross-section of the specimens during straining, which distinctly influence the force level and the strain to failure.

Tests in the rolling direction of the steel plates were performed in a universal testing machine, and the deformation rate was adjusted to give an initial strain rate of about $10^{-3}\ \mathrm{s}^{-1}$ independent of the specimen geometry. Three parallel tests were carried out for each combination of material and specimen geometry. During testing, the force was measured by the load cell of the testing machine, and the minimum cross-sectional diameters of the specimen were continuously measured in the transverse and normal directions of the plate using four displacement gauges mounted in a special device [21]. The latter gives a local measure of the specimen's deformation all the way to fracture, i.e., the average diameter reduction in the two directions, and is important for validation of fracture models.

3. Micromechanical modelling

The following modelling strategy is adopted to establish and validate a ductile fracture model for the three Weldox steels based on micromechanics and the use of a single uniaxial tension test per material.

1. A J_2 metal plasticity model is employed to describe the plastic behaviour of the three steel materials, where the experimental data from the uniaxial tension tests available in Dey et al. [21] are used for calibration of the model parameters.
2. Finite element simulations of an axisymmetric unit cell with a spherical void are used to calibrate a porous plasticity model for the three steels in the range of high stress triaxiality, where the already calibrated metal plasticity model is used to describe the matrix behaviour of the materials.

3. Strain localization analyses based on the imperfection band approach are conducted with metal plasticity outside and porous plasticity inside the band. Using metal plasticity outside the band is reasonable as we aim at calibrating an uncoupled plasticity and damage model. The void nucleation rate in the porous plasticity model is then determined to predict localization at the experimentally obtained fracture strain in uniaxial tension.
4. Using the calibrated metal and porous plasticity models, strain localization analyses are carried out to determine the fracture locus of the three steels under proportional loading in generalized axisymmetric tension for a wide range of stress triaxiality ratios.
5. Combining the fracture locus with a simple damage accumulation rule and the calibrated metal plasticity model, finite element simulations of ductile fracture in tension tests on smooth and notched specimens of the three steels are performed and compared with the experimental data from Dey et al. [21] to assess the accuracy of the proposed approach.

The modelling strategy is illustrated in Figure 2 using the same numbering as above. In the following, the different models combined in the micromechanics-based modelling approach of the three Weldox steels are described briefly.

3.1. Metal plasticity

Metal plasticity is described by the J_2 flow theory, see e.g. [35], where the von Mises yield criterion, the associated flow rule, and isotropic hardening are applied. The von Mises yield criterion is defined by $\Phi \equiv \sigma_{\mathrm{eq}} - \sigma_{\mathrm{M}} = 0$, where $\sigma_{\mathrm{eq}} = \sqrt{3\boldsymbol{\sigma}' : \boldsymbol{\sigma}'/2}$ is the von Mises equivalent stress and $\boldsymbol{\sigma}'$ is the deviatoric part of the Cauchy stress tensor $\boldsymbol{\sigma}$. The flow stress σ_{M} of the material is described by an extended Voce rule, $\sigma_{\mathrm{M}} = \sigma_0 + \sum_{i=1}^{2} Q_i(1 - \exp(-C_i p))$, where σ_0 is the initial yield stress, and Q_i and $C_i = \theta_i/Q_i$ are hardening parameters. The von Mises equivalent plastic strain is defined by $p = \int \sqrt{2\mathbf{D}^{\mathrm{p}} : \mathbf{D}^{\mathrm{p}}/3}\, dt$, where $\mathbf{D}^{\mathrm{p}}$ is the plastic rate-of-deformation tensor

given by the associated flow rule. The metal plasticity model is combined with isotropic elasticity defined by Young's modulus E and Poisson's ratio ν.

3.2. Porous plasticity

The Gurson model is adopted to describe porous plasticity including nucleation and growth of microscopic voids, while coalescence is not accounted for in the modelling [33]. The yield criterion is defined by [36][37]

$$\Phi = \left(\frac{\sigma_{\mathrm{eq}}}{\sigma_{\mathrm{M}}}\right)^2 + 2fq_1 \cosh\left(\frac{q_2}{2}\frac{\mathrm{tr}\boldsymbol{\sigma}}{\sigma_{\mathrm{M}}}\right) - (1 + q_3 f^2) = 0 \tag{1}$$

where f is the porosity (or void volume fraction), q_1, q_2, q_3 are the Tvergaard parameters [37], and σ_{M} is the flow stress of the matrix material, defined by the extended Voce rule. As for metal plasticity, the associated flow rule is adopted to define the plastic rate-of-deformation tensor $\mathbf{D}^{\mathrm{p}}$, and the porosity evolution is governed by

$$\dot{f} = (1 - f)\mathrm{tr}\mathbf{D}^{\mathrm{p}} + A_{\mathrm{n}}\dot{p} \tag{2}$$

where A_{n} governs the uniform nucleation of voids and the equivalent plastic strain p is defined by equating the plastic work in the matrix to the macroscopic plastic work [37]. The initial porosity is denoted f_0. The porous plasticity model is combined with isotropic elasticity defined by Young's modulus E and Poisson's ratio ν.

3.3. Unit cell simulations

An axisymmetric unit cell with an embedded spheroidal void is applied for the calibration of the porous plasticity model, see Figure 3, where x_1 and x_2 are in the lateral and axial direction of the unit cell, respectively. The geometry of the unit cell can be described by the cell aspect ratio, $\lambda = L_2/L_1$, the void aspect ratio, $w = r_2/r_1$, and the void volume fraction

$$f = \frac{2r_1^2 r_2}{3L_1^2 L_2} \tag{3}$$

where (L_1, L_2) are the outer dimensions of the unit cell and (r_1, r_2) are the semi-axes of the void along the two coordinate axes (x_1, x_2). The initial values of λ and w are set to unity, i.e., the cell

is equi-axed and the void is spherical. The macroscopic strains in the lateral and axial directions of the unit cell are given by [38][39]

$$E_{11} = \ln\left(\frac{L_1}{L_0}\right), \quad E_{22} = \ln\left(\frac{L_2}{L_0}\right), \quad E_{33} = E_{11} \tag{4}$$

where L_0 is the initial value of L_1 and L_2, and the macroscopic equivalent strain measure of the unit cell is defined as

$$E_{\mathrm{eq}} = \frac{2}{3}|E_{22} - E_{11}| \tag{5}$$

The macroscopic von Mises equivalent stress, Σ_{eq}, the hydrostatic stress, Σ_{h}, and the stress triaxiality ratio, T, are then defined by [38][39]

$$\Sigma_{\mathrm{eq}} = |\Sigma_{22} - \Sigma_{11}|, \quad \Sigma_{\mathrm{h}} = \frac{1}{3}(\Sigma_{22} + 2\Sigma_{11}), \quad T = \frac{\Sigma_{\mathrm{h}}}{\Sigma_{\mathrm{eq}}} = \frac{\Sigma_{22} + 2\Sigma_{11}}{3|\Sigma_{22} - \Sigma_{11}|} \tag{6}$$

where $\Sigma_{33} = \Sigma_{11}$ has been assumed. Only states of generalized axisymmetric tension will be considered here in which $\Sigma_{22} \geq \Sigma_{11} = \Sigma_{33}$. The stress triaxiality T is varied between simulations but kept constant during the loading of the unit cell to obtain proportional loading paths. The matrix of the unit cell is governed by J_2 flow theory as described above in Section 3.1. For further details regarding the unit cell simulations the reader is referred to Dæhli et al. [39].

3.4. Localization analyses

Following Rice [40], we consider a solid with an initial imperfection in the form of a thin planar band. The material outside the band is subjected to uniform deformation under quasi-static loading conditions. Both the materials inside and outside of the band are assumed to be homogeneous, but the properties of the material inside the band are assumed to differ slightly from those of the material outside. The unit normal of the imperfection band is denoted $\boldsymbol{n}$, and is obtained from its initial value $\boldsymbol{n}_0$ as [40]

$$\boldsymbol{n} = \frac{\boldsymbol{n}_0 \cdot \boldsymbol{F}^{-1}}{\|\boldsymbol{n}_0 \cdot \boldsymbol{F}^{-1}\|} \tag{7}$$

where $\boldsymbol{F}$ is the deformation gradient tensor. Compatibility across the imperfection band implies that

$$\boldsymbol{L}_{\mathrm{b}} = \boldsymbol{L} + \dot{\boldsymbol{q}} \otimes \boldsymbol{n} \tag{8}$$

where $\boldsymbol{L}$ and $\boldsymbol{L}_{\mathrm{b}}$ are the velocity gradient tensors respectively outside and inside the band, and $\dot{\boldsymbol{q}}$ is a vector that represents the non-uniformity across the band. Continuing equilibrium across the band can be expressed as

$$\boldsymbol{n} \cdot \dot{\boldsymbol{P}}_{\mathrm{b}} = \boldsymbol{n} \cdot \dot{\boldsymbol{P}} \tag{9}$$

where $\boldsymbol{P}$ and $\boldsymbol{P}_{\mathrm{b}}$ are the nominal stress tensors outside and inside the band, respectively, and the reference configuration is taken to coincide with the current configuration at any stage of the deformation process. Expressing the constitutive relations outside and inside the band as $\dot{\boldsymbol{P}} = \boldsymbol{C}^{\mathrm{t}} : \boldsymbol{L}$ and $\dot{\boldsymbol{P}}_{\mathrm{b}} = \boldsymbol{C}_{\mathrm{b}}^{\mathrm{t}} : \boldsymbol{L}_{b}$, we obtain an equation for $\dot{\boldsymbol{q}}$ as

$$(\boldsymbol{n} \cdot \boldsymbol{C}_{\mathrm{b}}^{\mathrm{t}} \cdot \boldsymbol{n}) \cdot \dot{\boldsymbol{q}} = \boldsymbol{n} \cdot (\boldsymbol{C}^{\mathrm{t}} - \boldsymbol{C}_{\mathrm{b}}^{\mathrm{t}}) : \boldsymbol{L} \tag{10}$$

where $\boldsymbol{A}_{\mathrm{b}}^{\mathrm{t}}(\boldsymbol{n}) = \boldsymbol{n} \cdot \boldsymbol{C}_{\mathrm{b}}^{\mathrm{t}} \cdot \boldsymbol{n}$ is the acoustic tensor of the band material, and $\boldsymbol{C}^{\mathrm{t}}$ and $\boldsymbol{C}_{\mathrm{b}}^{\mathrm{t}}$ are tangent modulus tensors for the material outside and inside the band, respectively (see [27] for details). The condition for localization is that the strain rate inside the band becomes infinite, which corresponds to $\det \boldsymbol{A}_{\mathrm{b}}^{\mathrm{t}}(\boldsymbol{n}) = 0$ for the first time. It should be noted that the critical orientation of the band normal is not known in advance, and localization analyses must be run for a wide range of orientations $\boldsymbol{n}_0$ to ensure that the ductility is minimized for the actual state of stress.

Strain softening is essential for the localization condition to be met for materials undergoing associated plastic flow, either only inside the band or outside the band as well. The Gurson model is employed in this study to describe strain softening inside the band, while metal plasticity is used for the material outside the band. The reader is referred to Morin et al. [27] for further details on the localization analysis by the imperfection band approach and the algorithms employed in the numerical implementation.

Localization analyses are performed here for two purposes: firstly, for the calibration of the void nucleation rate inside the imperfection band and, secondly, for the computation of the fracture locus. In the calibration of the nucleation rate of the porous plasticity model, the deformation history of the material outside the band is obtained by finite element simulations of the uniaxial

tension test with the J_2 plasticity model. Subsequently, a wide range of constant values of the stress triaxiality (i.e., proportional loading conditions) are prescribed for the material outside the band to determine parameters of the fracture model, considering again only states of generalized axisymmetric tension characterized by $\sigma_{\mathrm{I}} \geq \sigma_{\mathrm{II}} = \sigma_{\mathrm{III}}$, where $(\sigma_{\mathrm{I}}, \sigma_{\mathrm{II}}, \sigma_{\mathrm{III}})$ are the ordered principal Cauchy stresses.

3.5. Fracture model

The fracture locus obtained by the localization analyses is fitted by the expression [15][18]

$$p_{\mathrm{f}} = D_1 + D_2 \exp(D_3 T) \tag{11}$$

where p_{f} is the equivalent plastic strain at failure, T is the stress triaxiality ratio, defined by $T = \sigma_{\mathrm{h}}/\sigma_{\mathrm{eq}}$, $\sigma_{\mathrm{h}} = \frac{1}{3}\mathrm{tr}(\boldsymbol{\sigma})$ being the hydrostatic stress, and (D_1, D_2, D_3) are model parameters. The damage evolution rule is then taken as [18]

$$D = \int \frac{1}{p_{\mathrm{f}}} dp \leq 1 \tag{12}$$

where D is the damage variable and fracture is assumed to occur as D becomes equal to unity. As the fracture locus is valid only for proportional loading conditions [41], it follows that the effect of non-proportional loading is assumed described by the damage evolution rule. Finally, it should be noted that the proposed calibration method is not limited to the fracture model used in this study. This fracture model was selected because it was applied in finite element simulations by Dey et al. [21], using parameters identified directly from the experimental data, and it was deemed interesting to compare the fracture loci obtained with the two calibration methods.

4. Finite element procedures

4.1. Smooth and notched specimens

The smooth and notched tensile specimens were discretized with four-node bilinear axisymmetric elements with reduced integration and enhanced stiffness-based hourglass control (type CAX4R in Abaqus [42]). Exploiting the symmetry of the specimen geometry and loading conditions, only half of the specimen was modelled. The mesh was refined in the neck area of the smooth specimens and in the notch area of the notched specimens where the largest deformations were expected to

appear. The number of elements over the minimum cross-section radius was equal to 50 for all specimen types.

As an example, the mesh in the notch region of the specimen with notch radius 4 mm (R4) is shown in Figure 4. As illustrated in the figure, the mesh is graded in both the axial and radial directions to avoid excessive element distortion in the neck or notch region. The smallest elements in the neck or notch region have initial dimensions of 0.06 mm in the radial direction and 0.01 mm in the axial direction. Upon large plastic deformations, these elements will elongate significantly in the axial direction and contract in the radial direction, resulting in a good aspect ratio inside the neck or notch region at fracture, i.e., the elements are close to being quadratic in shape. Based on previous experiences of the authors with similar specimens it is assumed that the chosen mesh density should provide a converged solution for the plastic strain field in the neck region.

The explicit solver of Abaqus [42] was applied in the simulations of the tensile tests to allow for ductile fracture by element erosion. The loading was applied as a prescribed velocity at the extremity of the specimens. The prescribed velocity was ramped up with a smooth transition function over the first 5% of the step duration. Uniform mass scaling was applied to increase the stable time step in the simulations. It was checked that the kinetic energy was negligible compared with the internal energy in all simulations to ensure a quasi-static loading process.

The J_2 flow theory, as described in Section 3.1, was used in the simulations in combination with the fracture model presented in Section 3.5. The yield stress and hardening parameters for the three Weldox steels, based on the uniaxial tension tests presented in Dey et al. [21], are reported in Table 1 to Table 3. The Lüders plateau in the experimental stress-strain curves was neglected in the calibration of the extended Voce hardening rule, and as a result the fitted initial yield stress σ_0 is lower than the experimentally obtained yield stress, see [21] for details. However, as the main emphasis here is to describe ductile fracture, this simplification was deemed admissible. The parameters of the fracture model will be calibrated in Section 5.2. Ductile fracture is described by element erosion when the damage variable D equals unity.

4.2. Unit cell

The axisymmetric unit cell was discretized using the same elements as above, and the mesh is illustrated in Figure 3. Owing to the axial and radial symmetries, only half of the unit cell was

modelled. The number of elements over the edge of the void was equal to 30, which is deemed sufficient based on mesh convergence studies done in previous works [43].

The implicit solver of Abaqus [42] was used to perform the quasi-static simulations of the unit cell. A multi-point constraint routine, implemented by Dæhli et al. [39], was applied to keep the stress triaxiality constant and thus to obtain proportional loading by controlling the displacement of the outer walls of the unit cell. As already mentioned, simulations were performed in generalized tension only.

The J_2 flow theory was used to describe the behaviour of the matrix material in the unit cell with parameters given in Table 1 to Table 3 for the three Weldox steels.

5. Numerical simulations

5.1. Calibration of porous plasticity model from unit cell simulations

Unit cell simulations were performed to calibrate the Tvergaard parameters q_1, q_2, q_3 of the Gurson model in the range of high stress triaxiality. The initial porosity f_0 was set to 0.005, which is assumed to be an appropriate value for Weldox steels [13]. It has been shown previously that the Tvergaard parameters depend only weakly on the initial porosity used in the calibration process [33].

The unit cell was subjected to proportional loading in generalized tension with stress triaxiality ratio in the range $T \in [0.4, 0.5, \dots, 1.6]$. The macroscopic equivalent stress-strain curves and the evolution of porosity with the macroscopic equivalent strain were extracted from the simulations. These results are illustrated in Figure 5 for Weldox 700E. The strong influence of the stress triaxiality on the damage softening and strain to coalescence, as seen in Figure 5, was apparent for all three materials. The fracture loci obtained from the unit cell simulations are plotted in Figure 6, where the failure strain E_{f} is the macroscopic equivalent strain at void coalescence, assumed to take place when the global unit cell deformation shifts into a uniaxial straining mode. It is seen that the large difference in strength between the three steel materials only results in a small difference in the predicted fracture loci, at least for the assumed value of the initial porosity f_0. It should be noted here that the fracture strains observed experimentally for the three Weldox steels

were in about the same range as found in these simulations, which indicates that the initial porosity has a reasonable value.

The results from the unit cell simulations up to the onset of strain softening were used to find appropriate values of the Tvergaard parameters q_1, q_2, q_3 in the applied range of stress triaxiality ratios, assuming that $q_3 = q_1^2$, as proposed by Tvergaard [37]. The cost function used in the parameters optimization comprised two residuals, namely the strain-weighted average difference between the equivalent stress and the porosity from the unit cell simulations and the porous plasticity model, respectively, see Dæhli et al. [44] for details. In the current optimization, the residual in porosity was weighted 10 times higher than the residual in equivalent stress. The results from the unit cell simulations at the lowest stress triaxiality ratios were excluded from the optimization until an optimal solution was obtained giving values of q_1 greater than or equal to unity. The stress triaxiality ratios less than 0.8, 1.1. and 0.9 had to be left out of the calibration for Weldox 460E, Weldox 700E and Weldox 900E, respectively, to fulfil this constraint on the Tvergaard parameters. Using this approach, the Gurson model was calibrated for a range of stress triaxiality ratios relevant for the notched tensile specimens.

The resulting parameter values are given in Table 1 to Table 3. The response of the porous plasticity model and the unit cell simulations is compared in Figure 7 in terms of equivalent stress against equivalent strain for selected stress triaxiality ratios. In Figure 8, the porosity is plotted against equivalent strain for Weldox 700E for the same values of the stress triaxiality. Similar results are obtained for the two other materials. It should be noted that in these comparisons the equivalent plastic strain p is used for the Gurson model, while the macroscopic equivalent strain E_{eq} is applied for the unit cells. The difference between these two strain measures is expected to be small for the actual case. From the tables, it is seen that the Tvergaard parameters are close to unity and for the actual materials the original Gurson model would probably have given reasonably accurate results based on the unit cell simulations, the selected cost function and the applied constraints. It is seen from Figure 7 that the Gurson model overestimates the strain softening in the lower range of stress triaxiality ratios. As seen from Figure 8, the reason for this is that the Gurson model tends to overrate the void growth for the lowest stress triaxiality ratios compared with the unit cell simulations.

5.2. Fracture loci from localization analyses

Simulations of the tensile tests on smooth specimens were conducted for the three steels using the metal plasticity model. In these simulations, the specimens were deformed beyond fracture in the experiment. The deformation gradient history was then extracted from all elements across the minimum cross-section of the specimen inside the neck and used to drive the localization analyses by applying the metal plasticity model outside the band (globally) and the porous plasticity model inside the band (locally). The nucleation rate A_{n} of the porous plasticity model was then adjusted so that localization occurred inside the band at the diameter reduction giving ductile fracture of the smooth specimen. The initial porosity f_0 was set equal to zero in these simulations. It was found that the localization condition was always first attained in the central element inside the neck. This is as expected in a uniaxial tension test, owing to the higher stress triaxiality in the centre of the neck. The nucleation parameters thus obtained are given in Table 1 to Table 3.

With all the parameters of the porous plasticity model determined, localization analyses were carried out for the three steels under proportional loading conditions, i.e., with constant stress triaxiality in generalized axisymmetric tension. The stress triaxiality T was varied between 0.4 and 3.0 to determine a total of 23 points on the discrete fracture locus. Since the fracture locus was expected to be much steeper in the lower triaxiality range, a smaller interval between the points was applied for $T < 1$ to get a more accurate description of the fracture locus. Localization analyses giving a critical void volume fraction above 0.2 were discarded, because coalescence was not considered in the porous plasticity model. This approach resulted in the removal of some of the points on the discrete fracture locus obtained in the lower range of the triaxiality ($T < 0.7$). The resulting discrete failure loci are plotted in Figure 9. It is interesting to note that the loci for the Weldox 460E and Weldox 700E steels are almost coalescing, while the locus for Weldox 900E lies slightly below. Thus, the results from the localization analyses indicate that these steels have reasonably similar ductility even if the strength varies greatly between them. A similar conclusion was drawn from the unit cell simulations, see Figure 6, even if the initial porosity in these simulations was not calibrated to experiments. It is further notable that the discrete failure loci obtained here are rather different from the failure loci presented in Dey et al. [21], which were based on a direct calibration against the experimental data without numerical simulations.

The fracture model presented in Section 3.5 was then fitted to the discrete failure loci from the localization analyses. The results are shown in Figure 9 and it is evident that the agreement is good. The values of the damage parameters D_1, D_2, D_3 are compiled in Table 1 to Table 3.

5.3. Simulation of tension tests on smooth and notched specimens

Finally, simulations of the tensile tests with smooth and notched specimens were carried out using the uncoupled plasticity and fracture model with the calibrated parameters. The force versus diameter reduction curves from experiments and simulations are plotted in Figure 10 for the smooth specimens used in the calibration process of the various models and in Figure 11 for the notched specimens used for validation purposes. The curves from all repeat tests presented by Dey et al. [21] are plotted to display the scatter in the experimental results, whereas a representative test was used in the calibration. It should be noted that the experimental stress-strain curves exhibited a Lüders plateau which was neglected in the simulations, as the main emphasis is on describing ductile fracture. In these figures, also the point of fracture obtained by conducting localization analyses based on the deformation history of the critical element in the various specimens is shown for comparison. The filled circle designates failure in the FE simulation based on the uncoupled fracture model, whereas the open square indicates failure as predicted by localization analyses. The difference between these two fracture predictions is either due to the fracture locus not exactly reproducing the results from the localization analyses or that the damage accumulation rule is not fully capable of accounting for a non-proportional stress path. As will be shown below, the stress path is indeed non-proportional to various degree for all specimen geometries.

In most cases, the force levels predicted in the simulations are in good agreement with the experimental ones. The exceptions are the R0.8 and R0.4 tests on Weldox 900E for which the predictions markedly overestimate the force level. The reason for these deviations has not been established. With respect to ductility, it is found that the fracture model gives estimates in satisfactory agreement with the experiments, considering that the calibration procedure is based on one uniaxial tension test only. The ductility estimates are mostly conservative for Weldox 460E and consistently non-conservative for Weldox 900E, whereas the estimates for Weldox 700E are in excellent agreement with the test results. In most cases, the localization analyses predict fracture initiation in good agreement with the uncoupled fracture model. For the smooth tensile tests, the

localization analyses give results in better agreement with the experiments, which is expected as these tests were used for calibration of the imperfection inside the band.

To further illustrate the degree of agreement between experiments and finite element simulations, the diameter reduction at failure of the various specimens is plotted in Figure 12. For the experiments, all repeat tests are plotted to display the scatter. Using these diagrams, the mean absolute percentage error in the diameter reduction at failure was found to be 11.4%, 6.8% and 16.7% for Weldox 460E, Weldox 700E and Weldox 900E, respectively. The mean absolute percentage error $\bar{\epsilon}$ was calculated as

$$\bar{\epsilon} = \frac{100\%}{N_s} \sum_{i=1}^{N_s} \frac{1}{N_r} \sum_{j=1}^{N_r} \left| \frac{x_{i,j}^{\text{exp}} - x_i^{\text{sim}}}{x_i^{\text{sim}}} \right| \tag{13}$$

where N_s is the number of specimen types, N_r is the number of repeat tests, and x represents an experimental or simulated datapoint, in this case the diameter reduction at failure. The number of specimen types N_s equals 5, whereas the number of repeat tests N_r equals 3, except for the R08 specimen of Weldox 460 E where only 2 successful tests were reported in [21]. Note that as the ductility decreases with the introduction of a notch, the absolute percentage error will increase even in cases where the absolute error remains unchanged. Dey et al. [45] calibrated the Cockcroft-Latham fracture model for the three Weldox steels and used the calibrated fracture model in finite element simulations of the tensile tests on the smooth and notched specimens. The results obtained by Dey et al. [45] without use of finite element analysis in the calibration of the fracture model were significantly less accurate than those obtained here.

The evolution of the stress triaxiality in the critical element (i.e., the element that fails first) as function of the equivalent plastic strain is displayed in Figure 13 for the different Weldox 460E specimens. In the simulations, fracture was found to initialize in or near the centre of the neck or notch region independent of specimen geometry and material, and then the crack propagated towards the outer surface of the specimen. In contrast, the simulations performed by Børvik et al. [46] for Weldox 460E showed that fracture initiated at the notch root and propagated towards the centre for the specimen with the sharpest notch, whereas for the other specimen geometries fracture initiated in the centre. The crack propagation speed was slower for the smooth specimen than for the sharpest notches for which the failure was immediate. It is seen that all the strain paths are non-

proportional, but the strongest deviations from linearity are found for the smooth specimen, due to necking, and for the specimens with the sharpest notches.

6. Discussion

The calibration of the Tvergaard parameters q_1, q_2, q_3 from unit cell simulations resulted in values rather close to unity. This is a result of the constraint used in the optimization procedure, namely that we restricted q_1 and q_2 to be greater than or equal to unity. If this restriction is not used, the Gurson model allows porosity greater than unity before the material has lost all its load-carrying capacity, which is deemed unphysical. This constraint was fulfilled simply by discarding the unit cell simulations at the lower stress triaxiality levels, where the Gurson model is known to overestimate the void growth and the void shape has large effect on the behaviour. As a result, the calibrated Gurson model will give conservative results, i.e., the damage evolution will be overestimated, and the ductility underestimated, in this range of stress triaxiality. The void nucleation rate A_n is calibrated from the results of the uniaxial tension test, with stress triaxiality in the range where the Gurson model is conservative. As a result, the value of A_n will be somewhat underestimated to compensate for the overestimation of the damage evolution. A possible outcome of this would be that the ductility of the notched specimens should be generally overestimated, as the Gurson model is more accurate for higher stress triaxiality, but this is not seen from the results.

The formula adopted to describe the fracture locus, proposed Hancock and Mackenzie [15] and later adopted by Johnson and Cook [18], is found to give accurate results compared with the localization analyses, as seen from Figure 9. This figure also shows that the fracture loci for the three Weldox steels are rather similar, even if their strength is markedly different. The predicted ductility decreases with increasing strength, but the effect is small. In Dey et al. [21], the fracture locus was established based on the experimental fracture strains and estimates of the initial stress triaxiality using Bridgman analysis. Employing this approach, the fracture locus varied between the three materials and the shape of the fracture loci was significantly different from the shape obtained from the localization analyses. It is believed that the method used in the present study is more accurate as the spatial and temporal variations of the stress and strain fields are accounted for in the analysis. The similarity of the predicted failure loci for the three materials is somewhat surprising as the experiments show that the strain to fracture, obtained from measuring the area of the minimum cross-section, decreases with increasing yield strength [21]. However, it should be

noted that the measured strain to fracture depends on both the material ductility, as described in the simulations by the fracture locus for proportional loading, as well as the temporal and spatial distribution of the stress and strain fields. As the work hardening of the three materials is similar [21], a higher yield strength tends to give a stronger propensity for plastic instability and therefore a higher stress triaxiality in the critical element. The stress triaxiality history in the critical element of the smooth specimen is shown in Figure 14 for the three materials. It is evident that the stress triaxiality at a given equivalent plastic strain is higher for higher yield strength. Thus, the apparent difference in ductility between the three materials seen in the experiments is assumed to be partly caused by the difference in the plastic behaviour and partly by the difference in the strain to fracture under proportional loading, as illustrated by the computed fracture loci in Figure 9.

Even if the smooth tensile test specimens were used for calibration of the nucleation rate A_{n} in the porous plasticity model later used to predict fracture in the localization analyses, the ductility is generally overestimated in the simulation of these tests. The reason for this is twofold. Firstly, the fracture locus is uncertain for low stress triaxiality ratios because it was effectively calibrated using stress triaxiality ratios in the range $T \in [0.7, 3.0]$. In large parts of the tension test on the smooth specimen, T is below this range, making the damage accumulation uncertain. Secondly, the stress path is markedly non-linear for these tests, increasing from 1/3 initially to almost unity at fracture in the critical element. Thus, the results indicate that a more advanced damage accumulation rule could have improved the results obtained with the uncoupled plasticity and fracture model. It is important to note here that the localization analyses based on the deformation history in the critical elements give accurate estimates of the fracture points, verifying that the calibration process was conducted properly.

7. Concluding remarks

Uncoupled plasticity and fracture models for three structural steels, namely Weldox 460E, Weldox 700E and Weldox 900E, were calibrated based on a single uniaxial tension test and micromechanical simulations using unit cells, metal and porous plasticity, and localization theory. The fracture model consisted of a fracture locus and a damage evolution rule, and somewhat surprisingly, almost the same fracture locus was found for all three steels in the calibration process. The calibrated plasticity and fracture models were subsequently used in finite element simulations of tension tests on axisymmetric smooth and notched specimens, and the numerically and

experimentally obtained ductility, in terms of diameter reduction at fracture, was compared as a function of the stress triaxiality induced by the notches of different radius. The predicted ductility was in general somewhat conservative for Weldox 460E, accurate for Weldox 700E and non-conservative for Weldox 900E. The applied method is quite general and can be used for more advanced uncoupled fracture models, like the modified Mohr–Coulomb and the Hosford-Coulomb fracture models. It is believed that the method is well suited to reduce the experimental programme required to calibrate fracture models for design of structures against failure. However, the method relies heavily upon the prediction accuracy of the porous plasticity model used in the localization analyses. The calibration of more advanced fracture models, which incorporate Lode parameter dependence, requires a proper assessment of the porous plasticity model also for states of generalized compression and shear. Another important topic is to develop porous plasticity models that describe the ductility of materials at low stress triaxiality ratios more accurately.

Acknowledgement

The present work has been carried out with financial support from Centre of Advanced Structural Analysis (CASA), Centre for Research-based Innovation, at the Norwegian University of Science and Technology (NTNU) and the Research Council of Norway through project no. 237885 (CASA).

References

[1] A. Kane, T. Børvik, T. Berstad, A. Benallal, O.S. Hopperstad. Failure criteria with unilateral conditions for simulation of plate perforation. European Journal of Mechanics A/Solids 30 (2011) 468–476.

[2] V. Aune, G. Valsamos, F. Casadei, M. Langseth, T. Børvik. On the dynamic response of blast-loaded steel plates with and without pre-formed holes. International Journal of Impact Engineering 108 (2017) 27–46.

[3] M.A. Iqbal, K. Senthil, V. Madhu, N.K. Gupta. Oblique impact on single, layered and spaced mild steel targets by 7.62 AP projectiles. International Journal of Impact Engineering 110 (2017) 26–38.

[4] X. Xiao, Y. Wang, V.V. Vershinin, L. Chen, Y. Lou. Effect of Lode angle in predicting the ballistic resistance of Weldox 700 E steel plates struck by blunt projectiles. International Journal of Impact Engineering 128 (2019) 46–71.

[5] M. Dunand, D. Mohr. On the predictive capabilities of the shear modified Gurson and the modified Mohr–Coulomb fracture models over a wide range of stress triaxialities and Lode angles. Journal of the Mechanics and Physics of Solids 59 (2011) 1374–1394.

[6] Y. Bai, T. Wierzbicki. Application of extended Mohr–Coulomb criterion to ductile fracture. International Journal of Fracture 161 (2010) 1–20.

[7] K. Nahshon, J.W. Hutchinson. Modification of the Gurson model for shear failure. European Journal of Mechanics A/Solids 27 (2008) 1–17.

[8] K.L. Nielsen, V. Tvergaard. Ductile shear failure of plug failure of spot welds modeled by modified Gurson model. Engineering Fracture Mechanics 77 (2010) 1031–1047.

[9] E. Løhre Grimsmo, L.E. Bryhni Dæhli, O.S. Hopperstad, A. Aalberg, M. Langseth, A.H. Clausen. Numerical study of fillet welds subjected to quasi-static and impact loading. International Journal of Mechanical Sciences 131–132 (2017) 1092–1105.

[10] M. Cockcroft, D. Latham. Ductility and the workability of metals. Journal of the Institute of Metals 96 (1968) 33–39.

[11] M. Španiel, A. Prantl, J. Džugan, J. Ružička, M. Moravec, J. Kuželka. Calibration of fracture locus in scope of uncoupled elastic–plastic-ductile fracture material models. Advances in Engineering Software 72 (2014) 95–108.

[12] G. Le Roy, J.D. Embury, G. Edwards, M.F. Ashby. A model of ductile fracture based on the nucleation and growth of voids. Acta Metallurgica 29 (1981) 1509-1522.

[13] I. Barsoum, J. Faleskog. Rupture mechanisms in combined tension and shear—Experiments. International Journal of Solids and Structures 44 (2007) 1768–1786.

[14] I. Barsoum, J. Faleskog. Rupture mechanisms in combined tension and shear—Micromechanics. International Journal of Solids and Structures 44 (2007) 5481–5498.

[15] J.W. Hancock, A. Mackenzie. On the mechanisms of ductile failure in high-strength steels subjected to multi-axial stress-states. Journal of the Mechanics and Physics of Solids 24 (1976) 147–160.

[16] A.C. Mackenzie, J.W. Hancock, D.K. Brown. On the influence of state of stress on ductile failure initiation in high strength steels. Engineering Fracture Mechanics 9 (1977) 167–168.

[17] J.W. Hancock, D.K. Brown. On the role of strain and stress state in ductile failure. Journal of the Mechanics and Physics of Solids 31 (1983) 1–24.

[18] G.R. Johnson, W.H. Cook. Fracture characteristics of three metals subjected to various strains, strain rates, temperatures and pressures. Engineering Fracture Mechanics 21 (1985) 31–48.

[19] M.S. Mirza, D.C. Barton, P. Church. The effect of stress triaxiality and strain-rate on the fracture characteristics of ductile materials. Journal of Materials Science 31 (1996) 453–461.

[20] O.S. Hopperstad, T. Børvik, M. Langseth, K. Labibes, C. Albertini. On the influence of stress triaxiality and strain rate on the behaviour of a structural steel. Part I. Experiments. European Journal of Mechanics A/Solids 22 (2003) 1–13.

[21] S. Dey, T. Børvik, O.S. Hopperstad, J.R. Leinum, M. Langseth. The effect of target strength on the perforation of steel plates using three different projectile nose shapes. International Journal of Impact Engineering 30 (2004) 1005–1038.

[22] J. Faleskog, I. Barsoum. Tension–torsion fracture experiments—Part I: Experiments and a procedure to evaluate the equivalent plastic strain. International Journal of Solids and Structures 50 (2013) 4241–4257.

[23] R. Kiran, K. Khandelwal. Experimental studies and models for ductile fracture in ASTM A992 steels at high triaxiality. Journal of Structural Engineering 140 (2014) 04013044.

[24] S. Basu, A.A. Benzerga. On the path-dependence of the fracture locus in ductile materials: Experiments. International Journal of Solids and Structures 71 (2015) 79–90.

[25] I. Barsoum, J. Faleskog. Micromechanical analysis on the influence of the Lode parameter on void growth and coalescence. International Journal of Solids and Structures 48 (2011) 925–938.

[26] M. Dunand, D. Mohr. Effect of Lode parameter on plastic flow localization after proportional loading at low stress triaxialities. Journal of the Mechanics and Physics of Solids 66 (2014) 133–153.

[27] D. Morin, O.S. Hopperstad, A. Benallal. On the description of ductile fracture in metals by the strain localization theory. International Journal of Fracture 209 (2018) 27–51.

[28] D. Mohr, S.J. Marcadet. Micromechanically-motivated phenomenological Hosford–Coulomb model for predicting ductile fracture initiation at low stress triaxialities. International Journal of Solids and Structures 67–68 (2015) 40–55.

[29] G. Gruben, O.S. Hopperstad, T. Børvik. Evaluation of uncoupled ductile fracture criteria for the dual-phase steel Docol 600DL. International Journal of Mechanical Sciences 62 (2012) 133–146.

[30] G. Gruben, D. Morin, M. Langseth, O.S. Hopperstad. Strain localization and ductile fracture in advanced high-strength steel sheets. European Journal of Mechanics A/Solids 61 (2017) 315–329.

[31] C.C. Roth, D. Mohr. Ductile fracture experiments with locally proportional loading histories. International Journal of Plasticity 79 (2016) 328–354.

[32] M. Dunand, D. Mohr. Hybrid experimental–numerical analysis of basic ductile fracture experiments for sheet metals. International Journal of Solids and Structures 47 (2010) 1130–1143

[33] D. Morin, L.E. Dæhli, T. Børvik, A. Benallal, O.S. Hopperstad. Numerical study of ductile failure under non-proportional loading. European Journal of Mechanics/A Solids 74 (2019) 221–241.

[34] T. Børvik, O.S. Hopperstad, T. Berstad, M. Langseth. A computational model of viscoplasticity and ductile damage for impact and penetration. European Journal of Mechanics A/Solids 20 (2001) 685–712.

[35] J.C. Simo, R.L. Taylor. Consistent tangent operators for rate-independent elastoplasticity. Computer Methods in Applied Mechanics and Engineering 48 (1985) 101–118.

[36] A.L. Gurson. Continuum theory of ductile rupture by void nucleation and growth: Part I – Yield criteria and flow rules for porous ductile media. Journal of Engineering Materials and Technology 99 (1977) 2–15.

[37] V. Tvergaard. Influence of voids on shear band instabilities under plane strain conditions. International Journal of Fracture 17 (1981) 389–407.

[38] A.A. Benzerga, J.-B. Leblond. Ductile fracture by void growth to coalescence. Advances in Applied Mechanics 44 (2010) 169–305.

[39] L.E.B. Dæhli, T. Børvik, O.S. Hopperstad. Influence of loading path on ductile fracture of tensile specimens made from aluminium alloys. International Journal of Solids and Structures 88–89 (2016) 17–34.

[40] J. R. Rice. The localization of plastic deformation. In: Theoretical and Applied Mechanics (Proceedings of the 14th International Congress on Theoretical and Applied Mechanics, Delft, 1976, ed. W.T. Koiter), Vol. 1, North-Holland Publishing Co., 1976, 207–220.

[41] A.A. Benzerga, D. Surovik, S.M. Keralavarma. On the path-dependence of the fracture locus in ductile materials – Analysis. International Journal of Plasticity 37 (2012) 157–170.

[42] Abaqus. Version 6.14. Dassault Systèmes Simulia Corp., Providence, RI, USA 2013.

[43] M. Kristoffersen, T. Børvik, O.S. Hopperstad. Using unit cell simulations to investigate fracture due to compression–tension loading. Engineering Fracture Mechanics 162 (2016) 269–289.

[44] L.E.B. Dæhli, J. Faleskog, T. Børvik, O.S. Hopperstad. Unit cell simulations and porous plasticity modelling for strongly anisotropic FCC metals. European Journal of Mechanics A/Solids 65 (2017) 360–383.

[45] S. Dey, T. Børvik, O.S. Hopperstad, M. Langseth. On the influence of fracture criterion in projectile impact of steel plates. Computational Materials Science 38 (2006) 176–191.

[46] T. Børvik, O.S. Hopperstad, T. Berstad. On the influence of stress triaxiality and strain rate on the behaviour of a structural steel. Part II. Numerical study. European Journal of Mechanics – A/Solids 22 (2003) 15–32.

Tables

Table 1. Material parameters for Weldox 460E.

Elasticity and metal plasticity						
E (GPa)	ν	σ_0 (MPa)	Q_1 (MPa)	θ_1 (MPa)	Q_2 (MPa)	θ_2 (MPa)
210	0.3	415	220	4678	492	395
Fracture locus						
D_1			D_2		D_3	
0.065			8.48		-2.27	
Porous plasticity						
q_1		q_2		q_3	A_n	
1.004		1.043		1.008	0.0048	

Table 2. Material parameters for Weldox 700E.

Elasticity and metal plasticity						
E (GPa)	ν	σ_0 (MPa)	Q_1 (MPa)	θ_1 (MPa)	Q_2 (MPa)	θ_2 (MPa)
210	0.3	795	135	4681	2620	254
Fracture locus						
D_1			D_2		D_3	
0.050			9.25		-2.38	
Porous plasticity						
q_1		q_2		q_3	A_n	
1.079		1.091		1.164	0.0033	

Table 3. Material parameters for Weldox 900E.

Elasticity and metal plasticity						
E (GPa)	ν	σ_0 (MPa)	Q_1 (MPa)	θ_1 (MPa)	Q_2 (MPa)	θ_2 (MPa)
210	0.3	961	155	3000	10000	170
Fracture locus						
D_1			D_2		D_3	
0.055			10.14		-2.52	
Porous plasticity						
q_1		q_2		q_3	A_n	
1.079		1.100		1.165	0.0085	

Figures

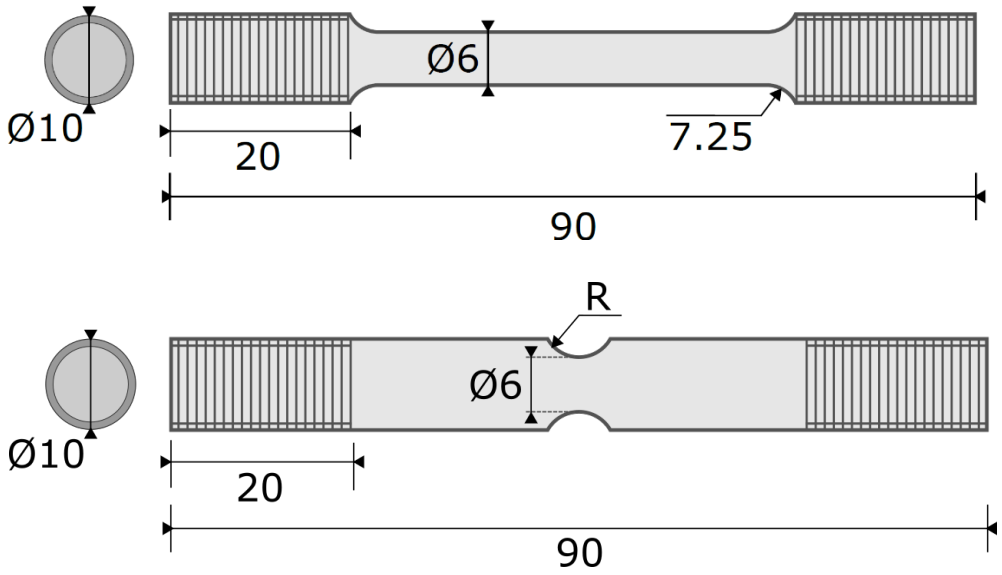

Figure 1. Geometry of the smooth and notched specimens with all measures in mm, where *R* equals 4 mm, 2 mm, 0.8 mm and 0.4 mm for the notched specimen. For manufacturing reasons, the side faces of the notch were inclined at an angle of 17.5° to the normal of the specimen axis for the specimens with notch radius 0.4 mm and 0.8 mm.

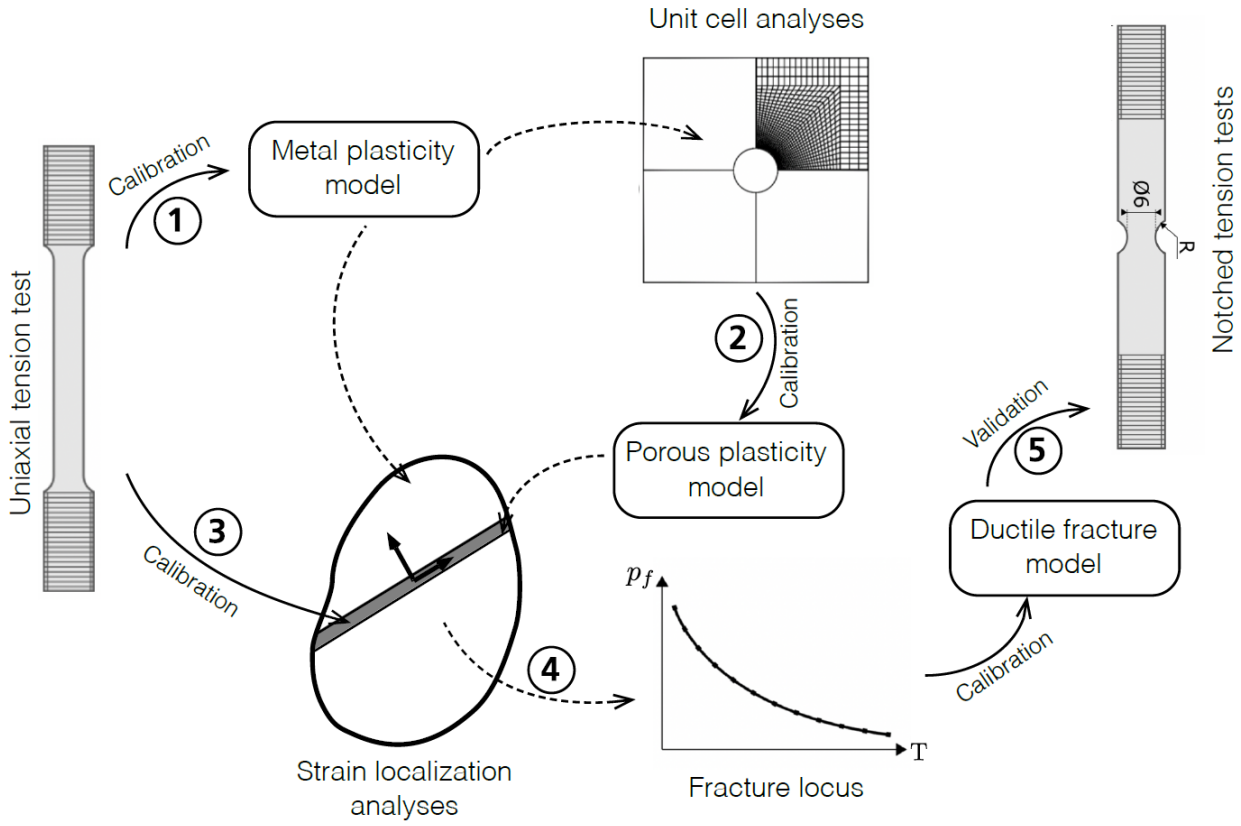

Figure 2. A conceptual description of the adopted micromechanics-based modelling framework used to establish the fracture locus of the three Weldox steels.

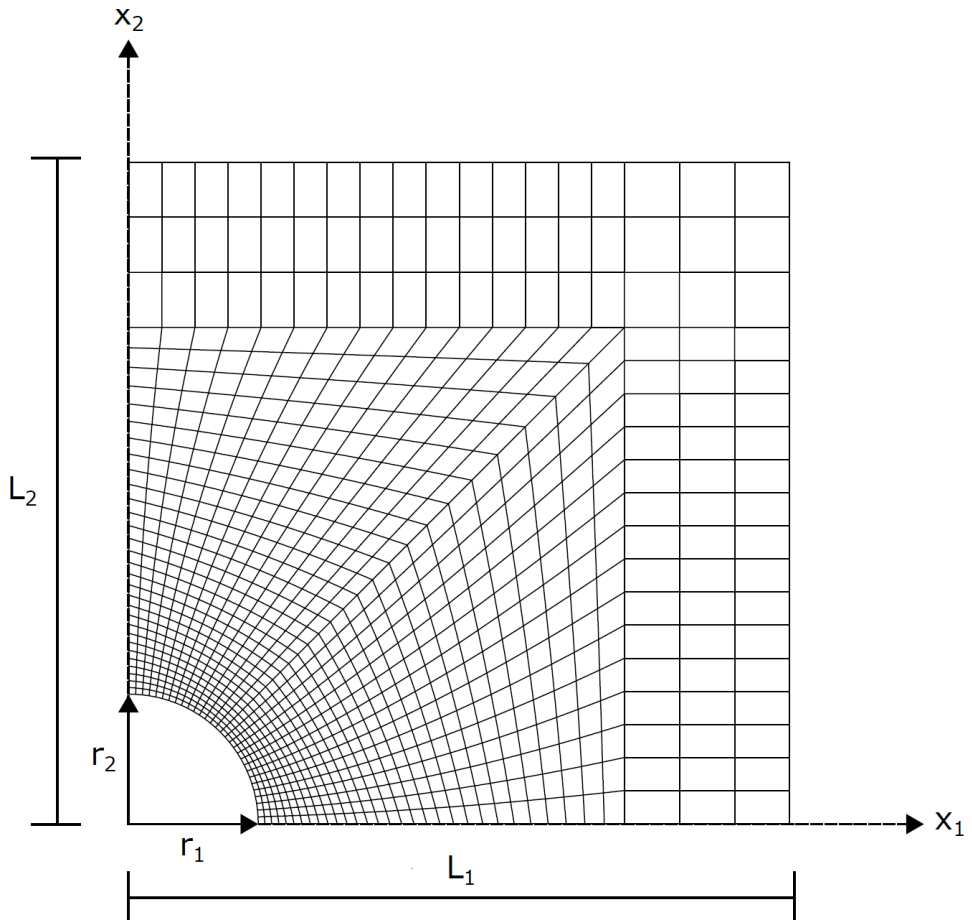

Figure 3. Geometry of axisymmetric unit cell and finite element mesh.

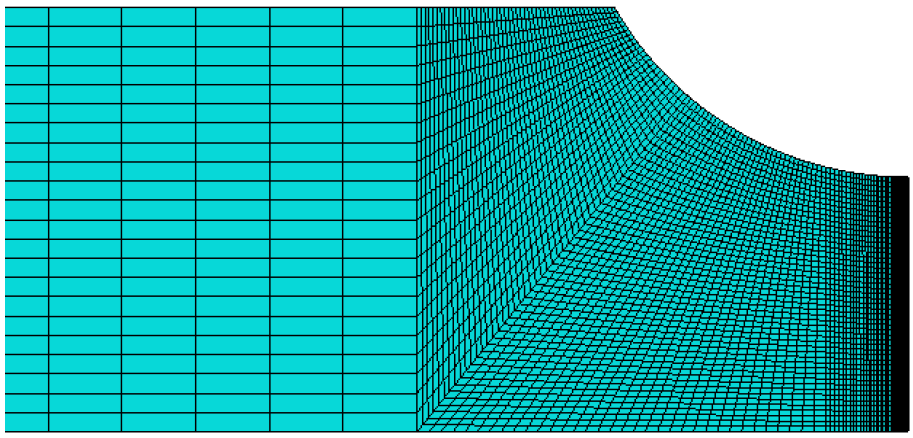

Figure 4. Details of the mesh in the notch region of the specimen with 4 mm notch radius.

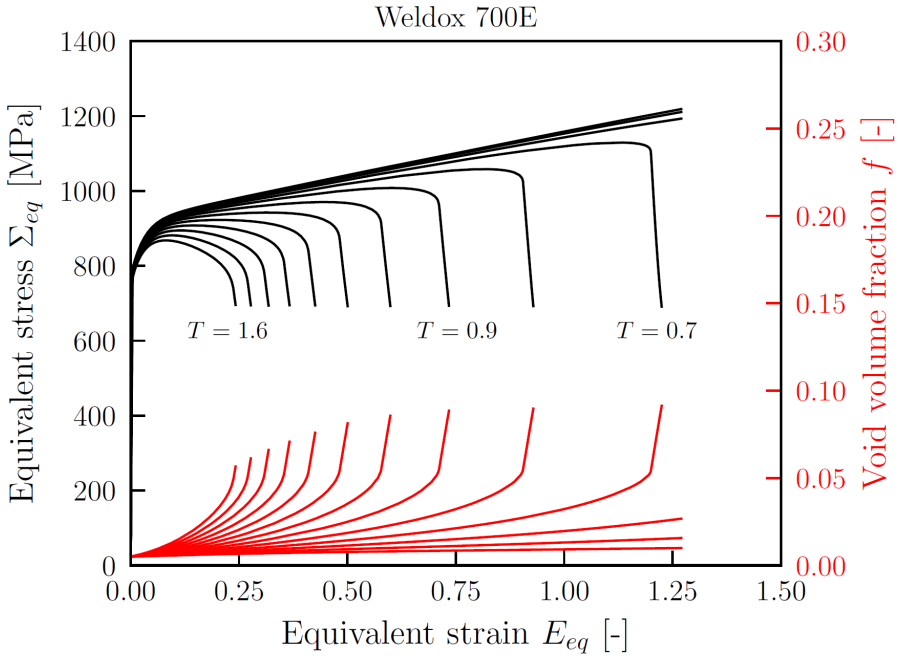

Figure 5. Macroscopic equivalent stress Σ_{eq} and void volume fraction f versus macroscopic equivalent strain E_{eq} for a range of stress triaxiality ratios T in unit cell simulations of Weldox 700E assuming an initial porosity of 0.5%.

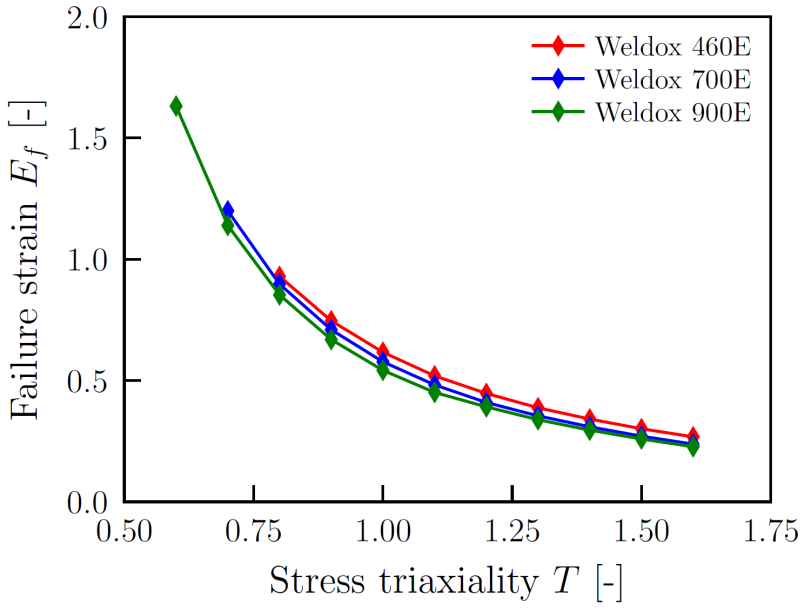

Figure 6. Computed fracture loci for the three Weldox materials based on unit cell simulations with an initial porosity of 0.5%, where the failure strain E_f is the value of the macroscopic equivalent strain E_{eq} at void coalescence.

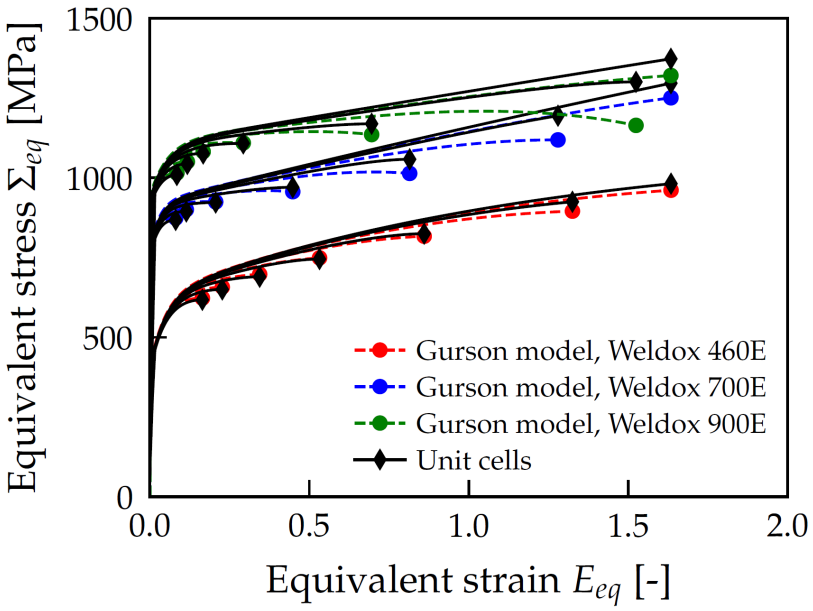

Figure 7. The global response of the calibrated Gurson model compared to the results obtained from the unit cell simulations for stress triaxiality $T = 0.4, 0.6, \ldots, 1.6$. The curves are plotted until incipient strain softening in the unit cell simulations.

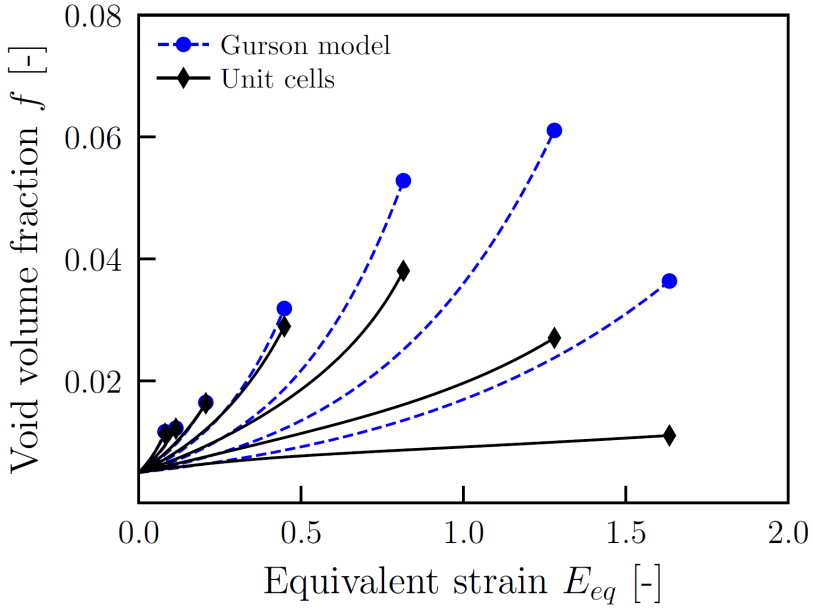

Figure 8. The evolution of the void volume fraction predicted by the calibrated Gurson model for Weldox 700E compared to the results obtained from the unit cell simulations for stress triaxiality $T = 0.4, 0.6, \ldots, 1.6$. The curves are plotted until incipient strain softening in the unit cell simulations.

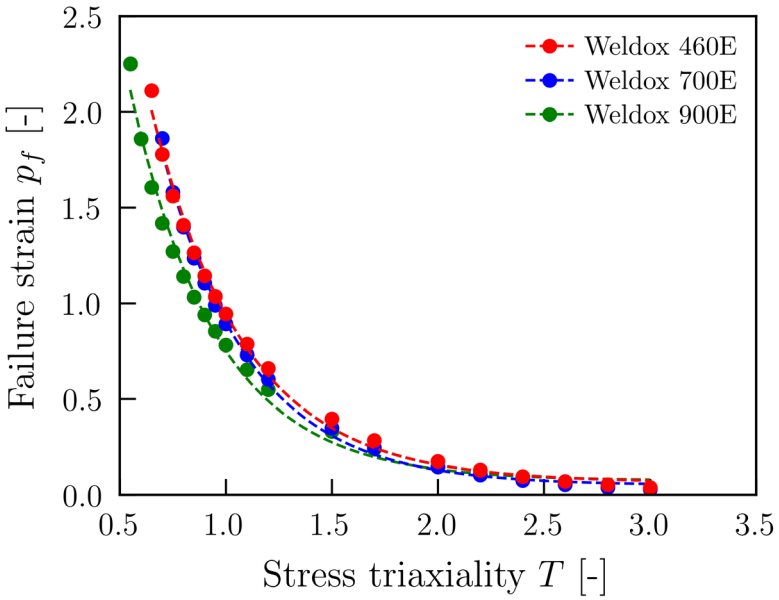

Figure 9. Computed fracture loci for the three Weldox materials, where the discrete points are based on the localization analyses and the dashed curves are based on Equation (11).

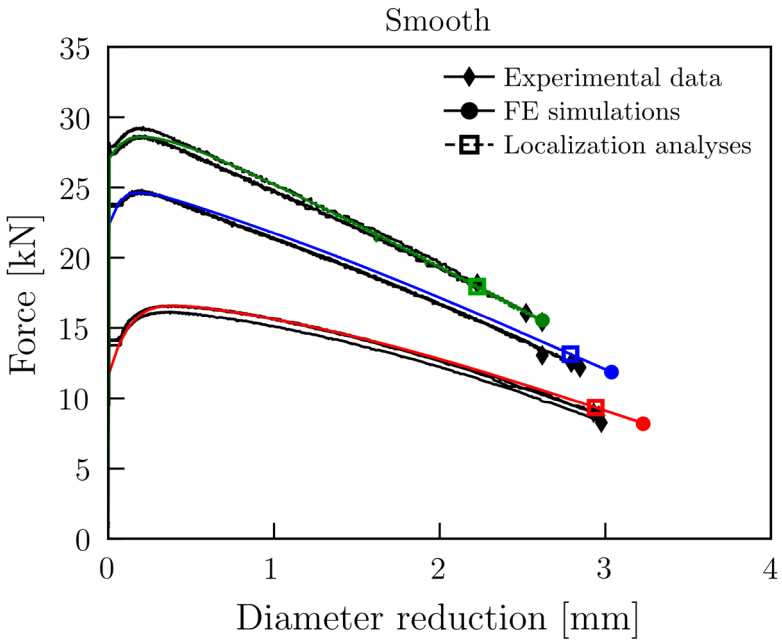

Figure 10. Comparison between experimental and numerical force versus diameter reduction curves to failure for the smooth tensile specimens of Weldox 460 E (lowermost, red curves), Weldox 700E (intermediate, blue curves) and Weldox 900E (uppermost, green curves) used in the calibration of the various models.

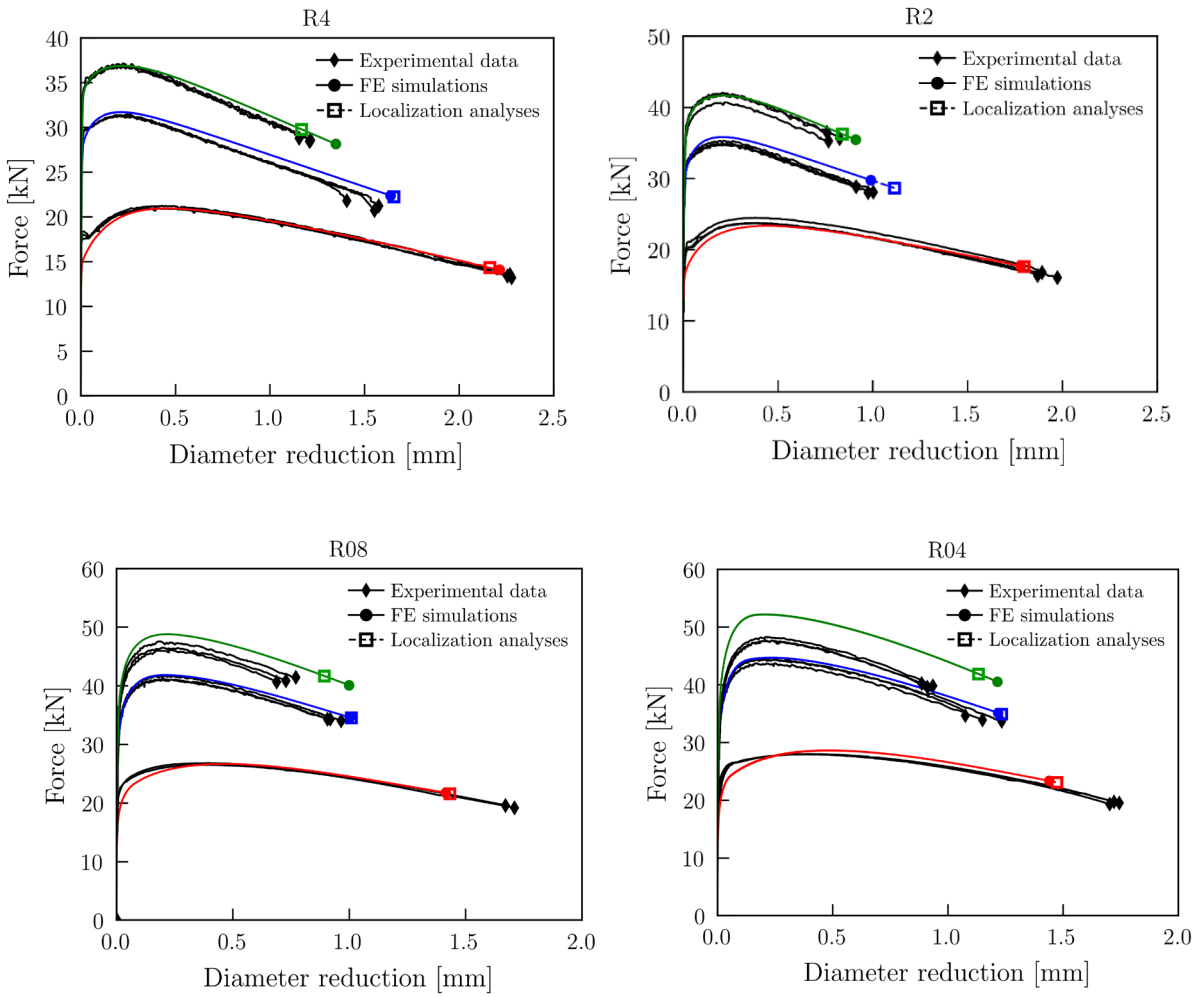

Figure 11. Comparison between experimental and numerical force versus diameter reduction curves to failure for the tensile tests on notched specimens of Weldox 460 E (lowermost, red curves), Weldox 700E (intermediate, blue curves) and Weldox 900E (uppermost, green curves), where R4, R2, R08 and R04 signify in turn specimens with notch radius 4 mm, 2 mm, 0.8 mm and 0.4 mm.

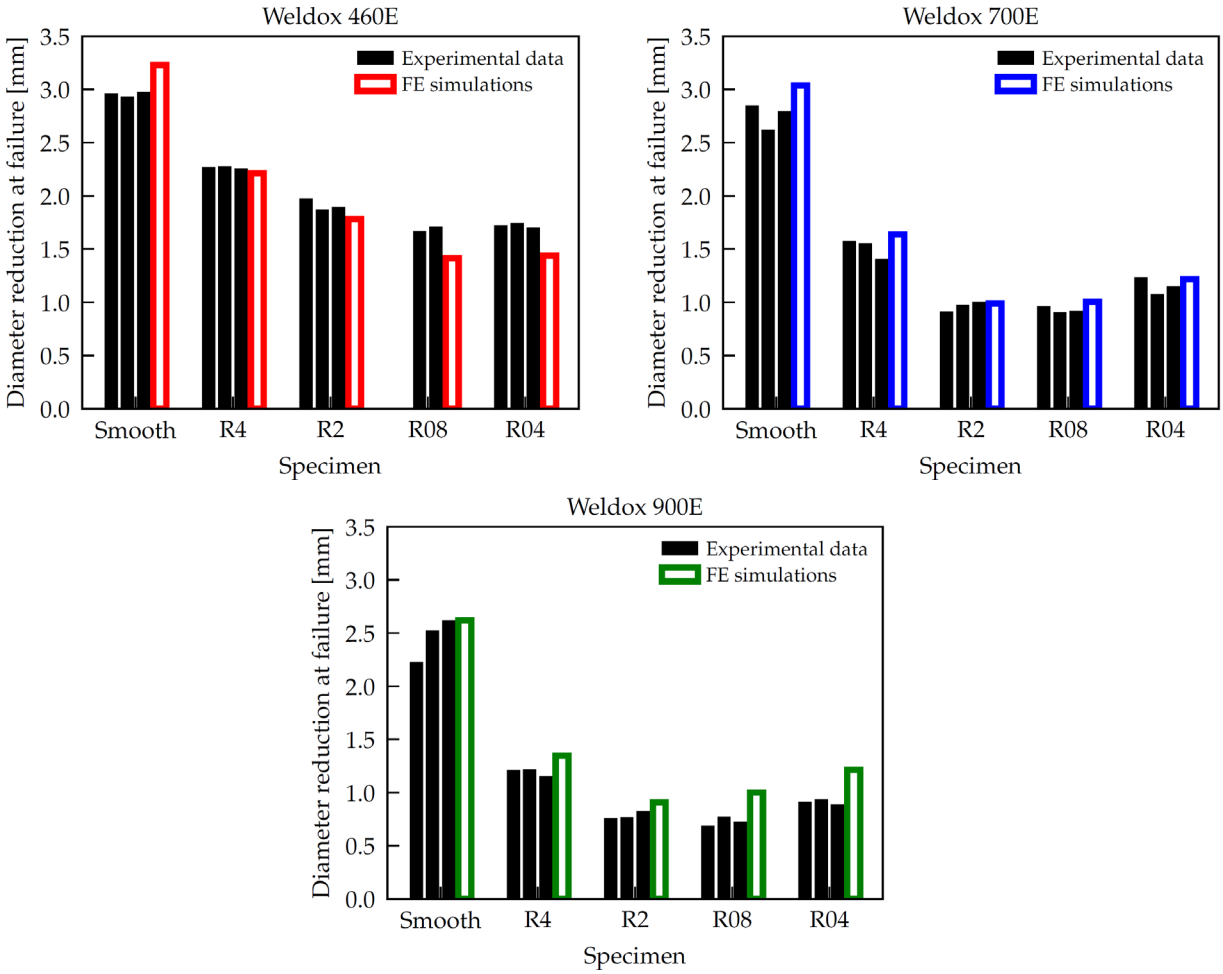

Figure 12. Diameter reduction at failure from experiments (all repeat tests) and finite element simulations. The initial nominal specimen diameter was 6 mm.

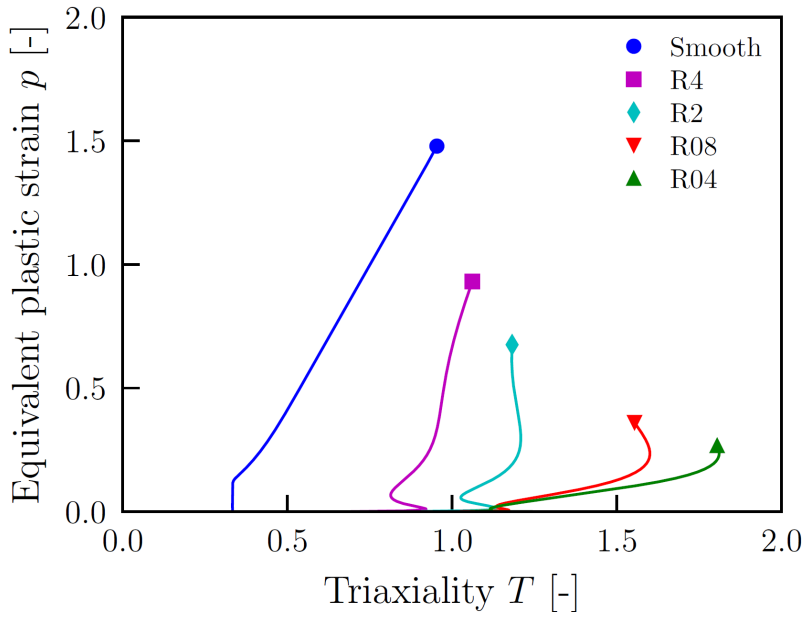

Figure 13. Evolution of stress triaxiality with equivalent plastic strain in the critical element for the different specimens of Weldox 460E.

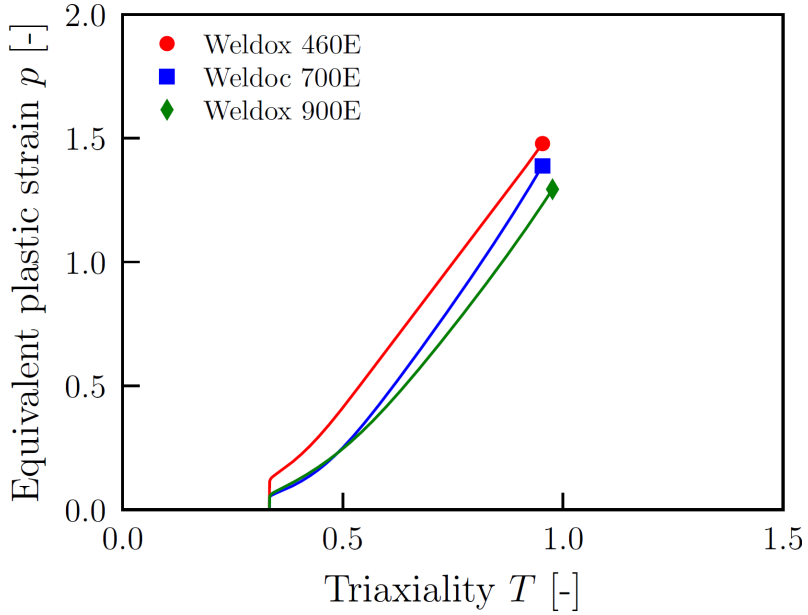

Figure 14. Comparison of the evolution of the stress triaxiality with equivalent plastic strain in the critical element for the smooth specimens of the three steels.